JGR Earth Surface

RESEARCH ARTICLE
10.1029/2021JF006289

Key Points:

- Seismic surveys of weathered material in the critical zone record magnitudes of seismic anisotropy as high as 36% and that vary with depth
- The fast direction of wave propagation in weathered materials aligns with the strike of foliation and fracture planes present in bedrock
- In situ weathering processes likely enhance the anisotropy already present in bedrock as it is exhumed toward the surface

Supporting Information:

Supporting Information may be found in the online version of this article.

Correspondence to:

J. L. Hayes,
hayesjo@dickinson.edu

Citation:

Eppinger, B. J., Hayes, J. L., Carr, B. J., Moon, S., Cosans, C. L., Holbrook, W. S., et al. (2021). Quantifying depth-dependent seismic anisotropy in the critical zone enhanced by weathering of a Piedmont schist. *Journal of Geophysical Research: Earth Surface*, *126*, e2021JF006289. https://doi.org/10.1029/2021JF006289

Received 28 MAY 2021
Accepted 20 SEP 2021

Quantifying Depth-Dependent Seismic Anisotropy in the Critical Zone Enhanced by Weathering of a Piedmont Schist

B. J. Eppinger[1], J. L. Hayes[1], B. J. Carr[2], S. Moon[3], C. L. Cosans[4], W. S. Holbrook[5], C. J. Harman[4], and Z. T. Plante[3]

[1]Department of Earth Sciences, Dickinson College, Carlisle, PA, USA, [2]Department of Geology and Geophysics, University of Wyoming, Laramie, WY, USA, [3]Department of Earth, Planetary, and Space Sciences, University of California, Los Angeles, Los Angeles, CA, USA, [4]Department of Environmental Health and Engineering, Johns Hopkins University, Baltimore, MD, USA, [5]Department of Geosciences, Virginia Polytechnic Institute and State University, Blacksburg, VA, USA

Abstract Weathering processes weaken and break apart rock, freeing nutrients and enhancing permeability through the subsurface. To better understand these processes, it is useful to constrain physical properties of materials derived from weathering within the critical zone. Foliated rocks exhibit permeability, strength and seismic anisotropy–the former two bear hydrological and geomorphological consequences while the latter is geophysically quantifiable. Each of these types of anisotropy are related to rock fabric (fractures and foliation); thus, characterizing weathering-dependent changes in rock fabric with depth may have a range of implications (e.g., landslide susceptibility, groundwater modeling, and landscape evolution). To better understand how weathering effects rock fabric, we quantify seismic anisotropy in saprolite and weathered bedrock within two catchments underlain by the Precambrian Loch Raven schist, located in Oregon Ridge Park, MD. Using circular geophone arrays and perpendicular seismic refraction profiles, anisotropy versus depth functions are created for material 0–25 m below ground surface (bgs). We find that anisotropy is relatively low (0%–15%) in the deepest material sampled (12–25 m bgs) but becomes more pronounced (29%–33%) at depths corresponding with saprolite and highly weathered bedrock (5–12 m bgs). At shallow soil depths (0–5 m bgs), material is seismically isotropic, indicating that mixing processes have destroyed parent fabric. Therefore, in situ weathering and anisotropy appear to be correlated, suggesting that in-place weathering amplifies the intrinsic anisotropy of bedrock.

Plain Language Summary The critical zone encompasses Earth's terrestrial surface where rock, water, soil, and biota interact to support life. Within the deeper reaches of the critical zone, rocks are subjected to weathering that transforms chemical and physical properties over time. As rocks weather, essential nutrients are released for use by organisms and space is opened within the rock allowing for water flow and storage. This study investigates how weathering and rock fabric interact. The term "rock fabric" refers to preexisting fractures and/or how minerals are organized within a rock. Schists, the rock type in this study, have a fabric with minerals made up of thin sheets, similar to a deck of cards. We examine how this rock fabric has been changed due to weathering by measuring the speed of sound waves that travel at different angles through weathered material close to the surface. Our data show that the fabric remains throughout much of the weathered material and may even become more pronounced as a result of weathering. Thus, the spacing between "cards" or the width of the fractures increases as rock is progressively weathered toward Earth's surface.

1. Introduction

Near-surface weathering processes drive porosity production and alter the hydraulic conductivity of subsurface materials. This ultimately determines the availability and movement of shallow groundwater resources (e.g., Klos et al., 2018; Meunier et al., 2007; Navarre-Sitchler et al., 2015). For this reason, numerous interdisciplinary studies have sought to understand and further constrain weathering in the shallow subsurface, often under the umbrella of critical zone (CZ) science, which focuses on the complex interactions between

rock, soil, air, and biota (e.g., Anderson et al., 2007; Brantley et al., 2007; Fletcher et al., 2006; Flinchum et al., 2018; Hayes et al., 2019; Holbrook et al., 2014, 2019). Recent research on this topic includes determining controls on CZ architecture, especially how weathering varies vertically and laterally beneath topography (e.g., Brantley et al., 2016; Harman & Cosans, 2019; Hayes et al., 2019; Holbrook et al., 2014, 2019; Moon et al., 2017; Rempe & Dietrich, 2014; Riebe et al., 2017; Sowards et al., 2018; St. Clair et al., 2015).

Although many studies have examined spatial variations in bulk weathering, it is still not fully understood how inherited rock fabric, specifically foliation and fractures in schists, are altered through weathering processes. Nonetheless, understanding how rock fabric is modified during weathering is important, particularly for hydrological purposes. For example, foliation, joints, and fracture networks have been shown to correlate with the directional hydraulic conductivity of their host media (Gerke & Vangenuchten, 1993; Neuman, 2005; Zimmerman & Bodvarsson, 1996), affect the infiltration rate of meteoric water (Leone et al., 2020), and act as the most prevalent sources of permeability in crystalline rocks (Nutter & Otton, 1969). Prior research has been primarily geared towards helping predict groundwater movement in unweathered bedrock. However, it is still unclear if these models can be extrapolated to overlying highly weathered saprolite, a critical groundwater reservoir in many ecosystems (e.g., Klos et al., 2018).

Past research highlights that foliation planes significantly influence how rock fabric changes during weathering. For example, sheet silicates such as biotite and muscovite, aligned parallel to foliation planes, expand perpendicular to their cleavage orientation while reacting with water to form clays (Rich, 1956). Internal stresses caused by the expansion of these minerals induce micro-fractures (Buss et al., 2008; Fordham, 1990; Shen et al., 2019), which act as a secondary rock fabric superimposed on top of foliation. There is also evidence that as schists weather, they become more susceptible to damage accrued via freeze-thaw and to a lesser extent, hydration-dehydration cycles (Fahey, 1983). However, there are not many observational studies that inform how weathering modifies rock fabric with indirect and non-invasive in situ measurements.

To quantify subsurface weathering, we constrain variations in seismic anisotropy from weathered bedrock to the surface, as this geophysical parameter is directly linked to the presence of rock fabric (foliation planes and fractures) (Crampin, 1984; Novitsky et al., 2018; Okaya & McEvilly, 2003). Novitsky et al. (2018) were the first to measure seismic anisotropy in the CZ using circular arrays of geophones. Their study took place within a granitic rock unit that bears a set of nearly vertical, northeast striking, tectonically induced fractures (Novitsky et al., 2018). At this site, Novitsky et al. (2018) found that the overlying saprolite exhibited anisotropy directionally similar to that of fractures in the underlying granite, implying that the saprolite retained the same fracture fabric found in the bedrock.

In this study, we expand the work of Novitsky et al. (2018) by constraining seismic anisotropy variations in saprolite derived from schist bedrock with intrinsic anisotropy. Such data fills an important knowledge gap: while numerous studies show that schists tend to be seismically anisotropic (e.g., Godfrey et al., 2000; Okaya & Christensen, 2002; Okaya & Mcevilly, 2003), fewer have measured seismic anisotropy in weathered schists (e.g., rock cores measured by Marques et al., 2010), and to our knowledge, none have measured seismic anisotropy in saprolite derived from the weathering of schist bedrock in situ. By measuring how seismic anisotropy varies with respect to depth, it will be possible to gauge how in-situ weathering affects the fabric of an intrinsically anisotropic rock.

2. Study Site and Geologic Setting

Located in Oregon Ridge Park, north of the Baltimore, MD, metropolitan area, the Pond Branch and Baisman Run catchments together span roughly 50 hectares (Figure 1). These catchments are entirely underlain by the Precambrian Loch Raven schist formation, which has a strong schistosity, is rich in micas, and exhibits garnet and staurolite porphyroblasts, indicating medium to high grade metamorphism (Cleaves et al., 1970; Duncan et al., 2013). The topography overlying the Loch Raven schist is characterized by incised streams where the relief of ridges and valleys ranges from 20 to 40 m.

Past research at Oregon Ridge Park has noted that base flow in streams is often sustained in the summer months, even during droughts (Cleaves et al., 1970). This has been attributed to large volumes of weathered material beneath ridges acting as effective groundwater reservoirs (Cleaves et al., 1970). Such findings

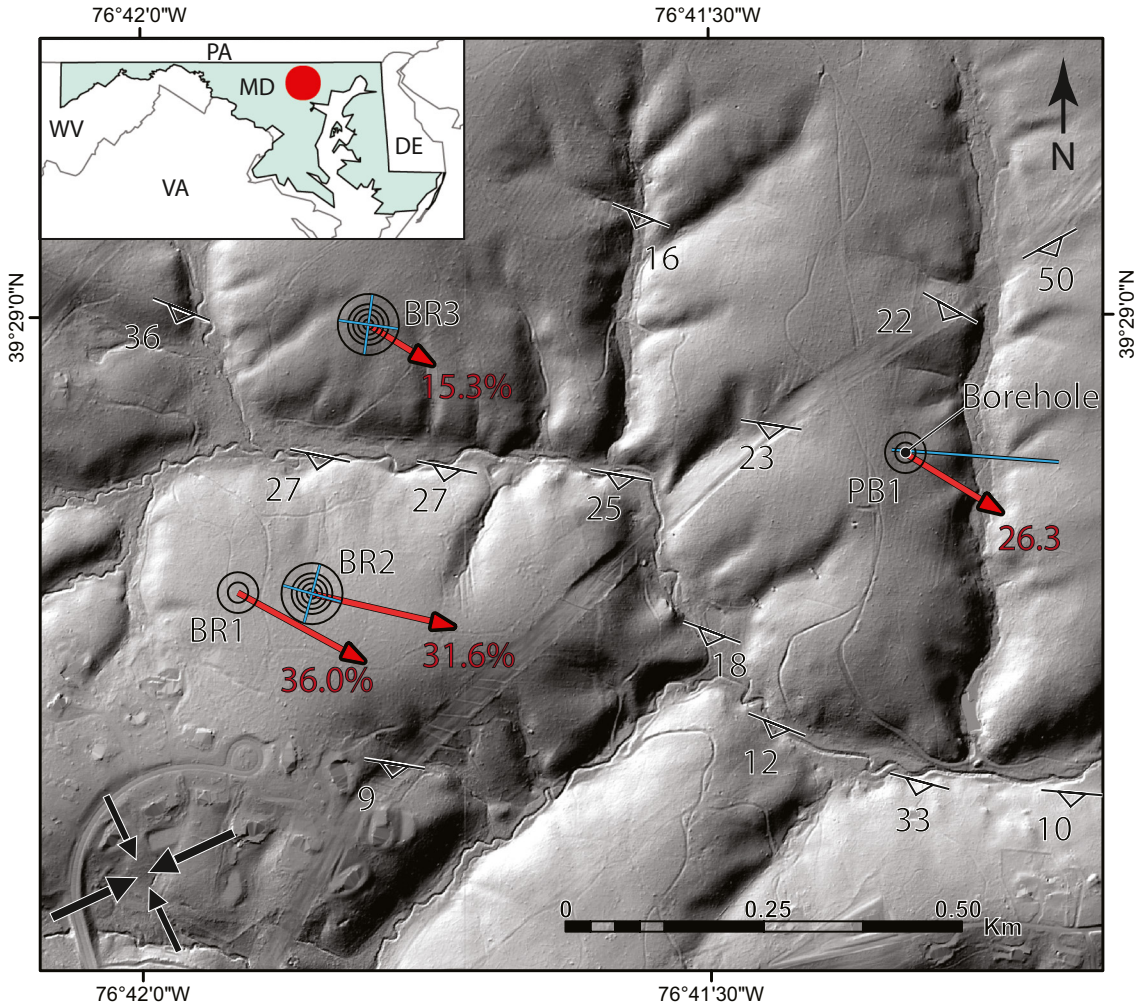

Figure 1. Field map of survey locations involved in this study, as well as an inset map indicating the general location of Oregon Ridge Park with respect to Maryland and the surrounding states. The base map is a hill-shade map generated from LIDAR data downloaded from imap.maryland.gov. Blue lines indicate the locations of 2-D seismic refraction profiles, including the eastern-most line, which represents the Pond Branch survey from St. Clair et al., (2015). Black circles indicate the locations of circular geophone arrays, and four groups of these arrays are labeled on the map and referred to by these names hereafter. Note that the map also indicates the location of a borehole which was installed and logged prior to this study at the center of the PB1 site. Red arrows indicate the fast directions of p-wave propagation measured with the 25 m circular arrays and are scaled to reflect the magnitude of the anisotropy measured. The magnitudes of anisotropy are also listed in red text below each arrow. The directions and lengths of black arrows in the bottom left corner indicate the directions and magnitudes of the most compressive (large arrows; N65°E, 10 MPa) and the least compressive (small arrows, N25°W, 3 MPa) tectonic stresses. Additionally, strike and dip measurements of foliation planes taken by Crowley et al. (1975) have been included.

agree with Nutters and Otton's (1969) claim that the occurrence of groundwater in this region is strongly governed by the thickness, porosity, and permeability of saprolite. The extent and volume of saprolite and weathered bedrock has been studied at the Pond Branch catchment by St. Clair et al. (2015), who conducted a seismic refraction survey crossing the main drainage. The results of this survey reveal deep weathering zones beneath ridgetops, where depth to bedrock may exceed 20 m below ground surface (bgs). However, these weathering zones pinch out toward valley bottoms, which often contain bedrock streams.

This type of CZ architecture, where the boundary between fracture-rich zones and intact bedrock mirrors surface topography, has been interpreted to result from the combined effects of topographic and strong regional compressive stresses (Moon et al., 2017; Slim et al., 2015; St. Clair et al., 2015). Both types of stresses are taken into account by topographic stress models, which can be used to predict the potential of opening-mode or shear fracturing (hereafter referred to as fracture potential) (Moon et al., 2017, 2020; Slim et al., 2015). Spatial variations in fracture potential and bulk weathering may correlate as stresses under

strong compression induce fracturing, create pathways for water to infiltrate, and initiate mineral dissolution (St. Clair et al., 2015). Along with initiating bulk weathering, fractures induced by topographic stresses alter rock fabric as a form of in situ weathering. Therefore, seismic anisotropy measurements in this study may also be sensitive to physical weathering brought on by topographic stresses acting on bedrock possessing intrinsic anisotropy.

3. Materials and Methods

To inform how inherited bedrock fabric changes during exhumation to the surface, this study utilizes two distinct seismic methods to measure anisotropy in the CZ. Seismic anisotropy is often measured by comparing the travel times or velocities of seismic energy propagating in multiple directions (e.g., Novitsky et al., 2018; Okaya & Mcevilly, 2003; Okaya & Christensen, 2002). In this study, seismic anisotropy is measured from travel times in circular geophone arrays and from velocity-depth functions in perpendicular seismic refraction profiles. To complement these non-invasive constraints on seismic anisotropy, we use optical and acoustic logs from a borehole at the PB1 site. These logs allow us to catalog rock fabric in competent rock and corroborate this data with collocated geophysical surveys.

3.1. Seismic Survey Design and Data Acquisition

3.1.1. Circular Arrays

Circular surveys were designed assuming a positive and monotonic velocity gradient, where seismic energy arriving at further offsets travels deeper. To characterize anisotropy variations with depth at a single location, it is necessary that each survey consists of nested circular geophone arrays, where sensors are offset from the center by fixed radii (Figure 1). In the two pilot studies conducted at the PB1 and BR1 sites, geophones were offset from a common center by 12.5 and 25 m, while subsequent circular surveys at the BR2 and BR3 sites also included offsets of 6.25, 18.75, and 37.5 m. Each circle was instrumented with two Geometrics geodes and forty-eight, 14-Hz geophones spaced at 7.5° increments. A 12 lb. sledgehammer impacting an aluminum plate was used as the seismic source at the center of the circles. Data from geophones were recorded after each swing individually rather than stacking consecutive swings. Before arriving at the field sites, the desired locations of geophones were pre-programmed into a Trimble robotic total station unit, which guided geophone placement in the field to within 5 cm of the desired location.

Results from circular surveys are most accurate when the topography of the site is planar (Novitsky et al., 2018). This ensures that the distance between the source and each receiver is equal and that variations in first arrival times are due to subsurface material properties e.g., stiffness parameters, porosity, mineralogy and saturation. To choose the locations of study sites, a sub-meter resolution DEM of Oregon Ridge Park (https://imap.maryland.gov/Pages/lidar-download-tool.aspx) was used to make a curvature map of the area. Locations with low curvature were usually restricted to hillslopes near ridge tops, and thus survey sites were placed in such areas. In the field, a base station was used to measure precise coordinates of survey locations. Then, the extent to which the topography of the study sites was planar was evaluated thoroughly by using a robotic total station to measure the northing, easting, and elevation (NEZ) coordinates of each geophone location, granted sighting of the target was possible through the trees. At the BR2 and BR3 sites, 50% and 86% of all geophone locations were surveyed respectively. These data points were then fitted with a plane and the goodness of the fit was evaluated through calculating the root-mean squared (RMS) residual (Figures S1 and S2).

3.1.2. Seismic Refraction Profiles

As another method of quantifying anisotropy, each survey also included two perpendicular 2D seismic refraction profiles: one in the slow and one in the fast direction of wave propagation determined from the circular array results. Orienting refraction surveys in the slow and fast direction is ideal because in these directions the group and phase velocities of arriving waveforms are equal. The required equipment again consisted of 48 geophones, an aluminum plate, and a sledgehammer. Geophone spacing and shot spacing were 1.5 and 3 m, respectively, and final shot-gathers were the result of automatically stacking five hammer swings. To increase maximum ray depth, shots off-line were also produced at locations extending 5, 10, and

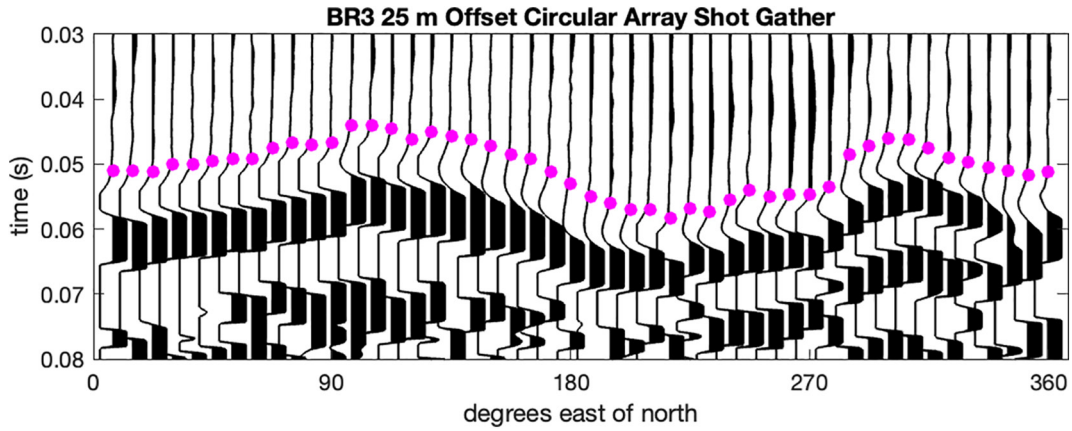

Figure 2. Example of a shot gather from the 25 m offset circular array at the BR3 site with first arrival picks marked as purple dots. Note the sinusoidal pattern in first arrival times and the high signal-to-noise ratio.

20 m from the first and last geophone, meaning that profiles were 110.5 m in total length. Topographic profiles used during the inversion of travel time data were extracted from surfaces generated by interpolating between NEZ data points collected with the total station (Figures S1 and S2).

3.2. Geophysical Data Reduction, Anisotropy Calculations, and Modeling

3.2.1. Circles

The eight shot gathers associated with each of the circular surveys were individually recorded and the least noisy 4–8 shots were stacked using Geogiga® software. After stacking the shots, the signal-to-noise ratio in the data was found to be high and the use of frequency filters were therefore unneeded for first-arrival picking. Pinpointing first arrivals involved identifying the earliest arriving set of waveforms with similar amplitude, polarity, and phase. First arriving waveforms were usually easy to identify, even for data from the farthest offsets, making the picking step straightforward (e.g., Figure 2). Travel time data was then exported to MATLAB, where anisotropy was quantified by fitting arrival times to a cosine function (Figure 3). The parameters (amplitude and phase shift) for these cosine functions were determined from solving a system of linear equations related to the data collected. A detailed formulation of these linear systems is included in the Supporting Information S1. Also included in the Supporting Information S1 are residuals between the fits and observed arrival times, which may be assessed to evaluate the degree to which the cosine model systematically misrepresents data (Figure S3)

The magnitude of anisotropy (A_t) was calculated using Equation 1 to compare the fastest and slowest fitted arrival times (T_{fast} and T_{slow}, respectively) (Birch, 1960; Novitsky et al., 2018). Note that the subscript "t" emphasizes that these anisotropy magnitudes were calculated by comparing travel times. The fitted cosine functions were also used to calculate azimuthal orientations of the fast direction of anisotropy (Figure 1 & Table 1).

$$A_t = \frac{T_{fast} - T_{slow}}{\frac{1}{2}\left(T_{fast} + T_{slow}\right)} * 100\% \quad (1)$$

To evaluate the error in anisotropy calculations, statistical tests similar to those employed by Novitsky et al. (2018) and Sacchi (1998) were used. These tests involved as series of trials where during each trial, half of the travel times were randomly removed. The remaining half of the travel times were fit with a cosine function which was used to quantify the magnitude of anisotropy in that trial. This process of randomly removing half and fitting the remaining travel times was applied to data from each circular survey for 500 trials. Using the results from all the trials, we calculated the mean value of A_t measured with each circle, as well as the variances associated with each mean (Table 1).

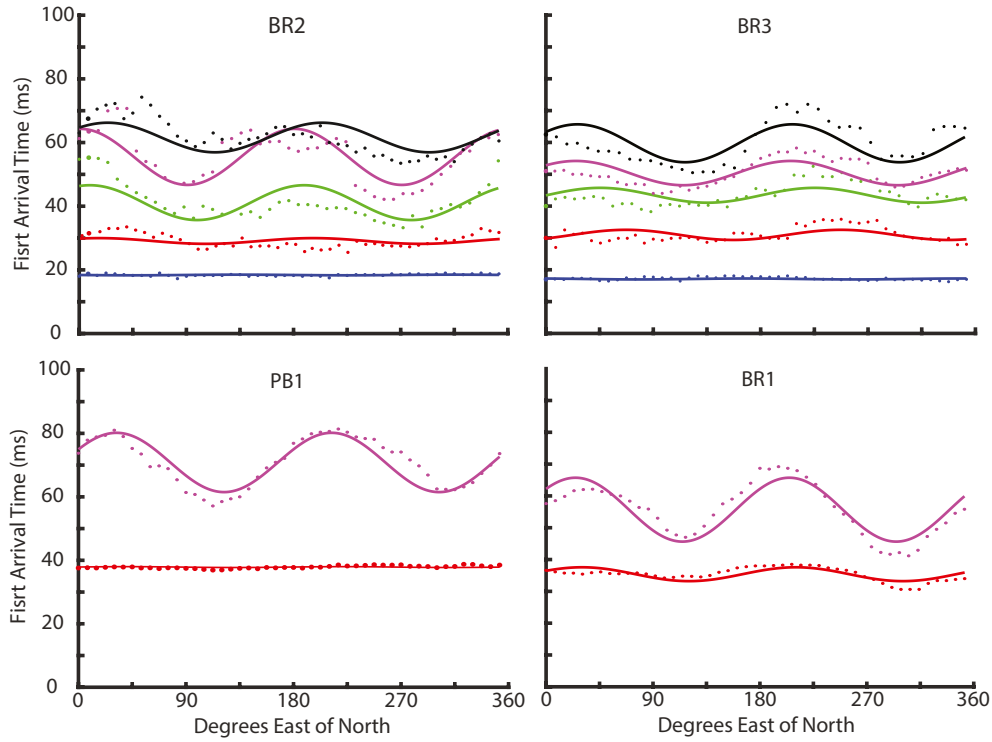

Figure 3. First arrival times and fitted cosine function from each survey site. First arrivals and fits are colored according to the radius of the survey with blue, red, green, purple, and black corresponding to 6.25, 12.5, 18.75, 25, and 37.5 m offsets respectively. R^2 values for fits can be found in Table 1.

3.2.2. Refraction Tomography

When analyzing data from the profile surveys, Geogiga® software were again used for picking first arrival times as well as for inverse modeling used to create tomograms. Geogiga®'s inversion algorithm allows the user to apply different smoothing parameters in the horizontal and vertical directions as well as minimum and maximum allowable velocities. All inversions involved in this study were implemented with identical parameters, including horizontal and vertical smoothing weights of 7.5 and 1.875 m respectively, while allowable velocities were constrained within 400–6,000 m/s. This velocity range spans estimates of velocities for unsaturated soil and crystalline rocks at low pressures, respectively (Barton, 2006). The model grid spacing is 0.750 and 0.375 m in the horizontal and vertical directions respectively for all tomograms.

Model sensitivity was assessed by using nine different initial models to produce nine separate test inversions for each of the four lines (e.g., Flinchum et al., 2018). Each test inversion involved 10 iterations and a model depth of 50 m; however, this depth was trimmed as to not exceed the deepest ray coverage. The initial model used and the resultant RMS error after 10 iterations corresponding to all 36 test inversions (9 inversions for each line) are recorded in Table S1. The final tomogram for each line as seen in Figure 4 is the average of the nine test inversions. Only model elements that are defined for all nine test inversions are defined in the final model. Likewise, the standard deviation, S, at each model element associated with the average of the nine test models was also calculated (Figure S4). The velocity depth profiles where crossing tomograms intersect (Figures S5 and S6) were extracted and then used to calculate

Table 1
Radial Anisotropy Survey Results

Site	Radius (m)	% Anisotropy	Fast direction orientation (°)	R^2 value for fit
BR1	12.5	12.3 ± 0.137	118	0.574
BR1	25	36.0 ± 0.375	117.4	0.798
BR2	6.25	1.48 ± 0.660	45.0	0.0402
BR2	12.5	6.99 ± 2.86	105.0	0.0846
BR2	18.75	26.5 ± 5.06	100.0	0.459
BR2	25	31.6 ± 3.35	92.0	0.623
BR2	37.5	15.2 ± 2.60	112.5	0.382
BR3	6.25	2.11 ± 0.989	75.0	0.0575
BR3	12.5	10.6 ± 3.10	157.5	0.221
BR3	18.75	10.9 ± 3.00	136.0	0.226
BR3	25	15.3 ± 2.34	112.5	0.474
BR3	37.5	20.2 ± 3.40	118.5	0.445
PB1	12.5	0.695 ± 0.0893	127.5	0.0428
PB1	25	26.3 ± 0.298	120.0	0.813

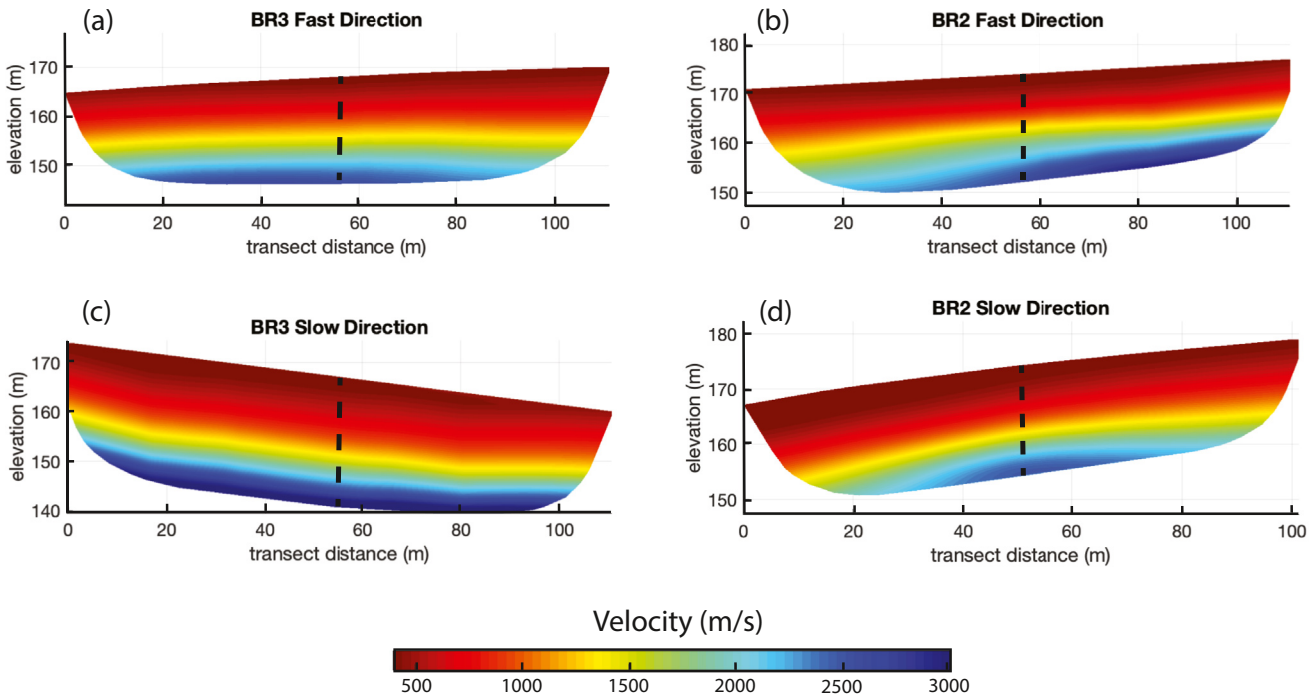

Figure 4. Tomograms used to calculate A_v colored for velocity. Note that seismic lines from the same site intersect halfway along their transects. The points of intersection are denoted by dashed black lines. Also note that the middles of intersecting tomograms from (a) and (c) are compared to calculate the blue curve while those from (b) and (d) are compared to calculate the red curve in Figure 5b.

percent anisotropy A_v via Equation 2 (Birch, 1960), where the subscript denotes that these anisotropy values were calculated by comparing velocities. Standard deviation values were also extracted where crossing tomograms intersect and used to estimate an envelope of reasonable A_v values. The bounds of this envelope are defined using Equations 3 and 4.

$$A_v = \frac{V_{fast} - V_{slow}}{\frac{1}{2}\left(V_{fast} + V_{slow}\right)} * 100\% \tag{2}$$

$$A_v^{upper} = \frac{\left(V_{fast} + S_{fast}\right) - \left(V_{slow} - S_{slow}\right)}{\frac{1}{2}\left[\left(V_{fast} + S_{fast}\right) + \left(V_{slow} - S_{slow}\right)\right]} * 100\% \tag{3}$$

$$A_v^{lower} = \frac{\left(V_{fast} - S_{fast}\right) - \left(V_{slow} + S_{slow}\right)}{\frac{1}{2}\left[\left(V_{fast} - S_{fast}\right) + \left(V_{slow} + S_{slow}\right)\right]} * 100\% \tag{4}$$

3.3. Transforming Travel Time Estimates of Anisotropy From Radial Offset to Depth Space

To transform the results of radial seismic anisotropy surveys from functions of offset to functions of depth, a mapping of ray depth to offset is required. To produce this mapping, seismic rays are traced through the averaged velocity models used to calculate A_v. Hence, each site has two velocity models associated with it - one based on the profile in the fast direction and another based on the profile in the slow direction. It is of primary importance to estimate ray paths in these directions because rays tend to travel deepest in the slow model and shallowest in the fast model. Therefore, estimating raypaths with these models provides an upper and lower bound on ray depth at a given offset. These ranges are represented by the vertical error bars in Figure 5a.

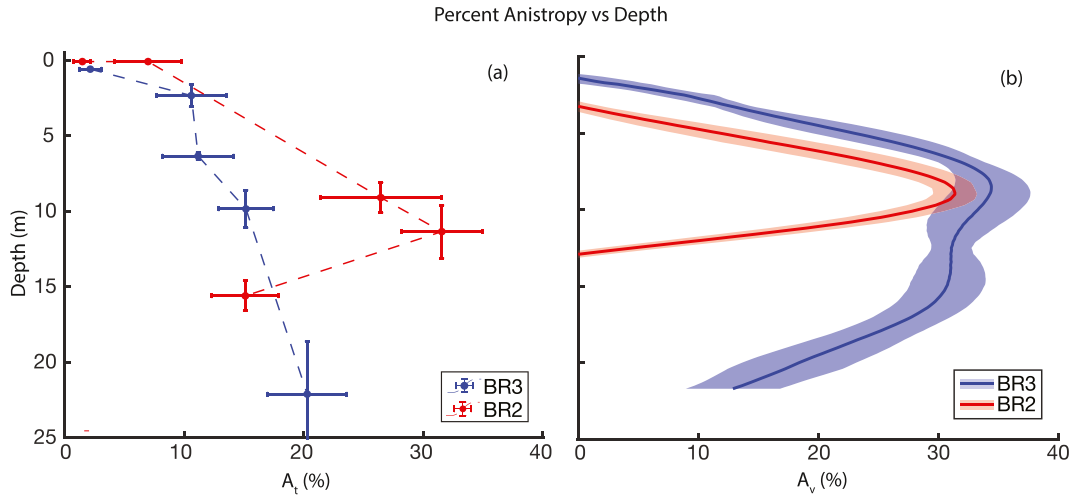

Figure 5. (a) Anisotropy versus depth functions calculated by comparing arrival times measured with radial surveys. Ray tracing through velocity models allow for data to be plotted as a function of depth. Vertical error bars indicate the range in ray depths between the fast and slow velocity models. Lateral error bars indicate the standard deviation of averaged percent anisotropy magnitudes after 500 bootstrapping iterations. (b) Positive anisotropy versus depth functions calculated by comparing velocity depth profiles at the middles of intersecting tomograms. Solid lines (red or blue depending on the site) indicate direct comparisons between the values for the fast and slow directions. The shaded envelopes encompass ranges of anisotropy values that are believed to be statistically reasonable. These envelopes help account for variance across test inversions and are calculated using Equations 3 and 4.

3.4. Borehole Data Collection

Because the presence of rock fabrics such as foliation and fractures can result in seismic anisotropy (e.g., Crampin et al., 1980; Novitsky et al., 2018; Okaya & Christensen, 2002; Okaya & Mcevilly, 2003), it is helpful to catalog them throughout the shallow subsurface. We do this using a borehole adjacent to the PB1 site where down-hole imaging logs were collected in 2019. These imaging logs include both optical (photogrammetry) and single-component acoustic televiewer data. Such data helps characterize the fabric of competent rock through which seismic energy propagates during the collocated anisotropy surveys. In particular, three types of features are distinguished using optical and acoustic logs of the borehole: foliation planes and two classes of fractures. The first class of fractures (also referred to as class I) relates to failure along or subparallel to foliation planes, while the second (also referred to as class II) corresponds to fractures that have relatively large apertures and usually crosscut foliation at steeper angles. For this study, we use data collected from 18.5 to 30.5 m bgs, corresponding to the depth where material can be cored by drilling (below which, optical and acoustic logs are available) and the inferred maximum depth of sensitivity to our geophysical surveys, respectively.

4. Results

4.1. Magnitude & Direction of Anisotropy Revealed by Circle Surveys

The fast directions of p-wave propagation for surveys recording significant magnitudes of radial anisotropy ($A_t > 15\%$) range between N92ºE and N120ºE, approximately parallel to the strike of the foliation planes in the schist bedrock (Figures 1–3 & Table 1). For surveys from the PB1 and BR1 sites, the degree of seismic anisotropy is larger in the 25 m radius surveys than in the 12.5 m radius surveys. Thus, it is inferred that at these sites, the degree of anisotropy increases with depth, with higher magnitudes of anisotropy (up to 36.0%) observed at the BR1 site.

Data from radial anisotropy surveys conducted at the BR3 site (blue curve in Figure 5a) generally agree with trends found in data collected at PB1 and BR1. These surveys show that the magnitude of anisotropy increases with offset, where increasing offset is a proxy for deeper ray coverage (Figure 3). With five data points from BR3 sites (cf., two points in BR1 site), anisotropy variations with offset and by extension depth

are better constrained. The greatest jump in anisotropy occurs between the 6.25 and 12.5 m offsets (Table 1). Between the 12.5 and 25 m offsets, the magnitude of anisotropy increases slightly or stays constant, increasing significantly again between the 25 and 37.5 m offsets where a maximum of 20% anisotropy is reached.

Radial anisotropy surveys located at the BR2 site (red curve in Figure 5a) differ from all previously mentioned data in that the magnitude of anisotropy does not increase monotonically with offset. The highest magnitudes of anisotropy in these surveys correspond to the 18.75 and 25 m offsets (Table 1). A maximum magnitude of anisotropy of 32% at this site exceeds the highest magnitudes associated with the surveys located at the BR1 and PB1 sites. Magnitudes of anisotropy calculated from the 6.25 m, 12.5 m, and 37.5 m offsets tend to be slightly lower than anisotropy magnitudes calculated for surveys of the same offset located at BR2.

With circular surveys, the topographic surface can alter p-wave arrival times if it deviates from being planar. Fortunately, due to our careful placement of circular arrays, the topography at the BR3 and BR2 sites fit planar surfaces well (Figures S1 and S2). For instance, the median absolute value of residuals between the measured elevation points and the fitted planar surface at the BR3 and BR2 sites were 0.096 and 0.095 m respectively. Keeping these figures in mind, and assuming an average subsurface velocity of 1,000 to 2,000 m/s means that typical deviations in p -wave arrival times caused by non-planar topography are on the order of 0.1 to 0.05 ms. Such values are small compared the observed arrival times and are likely less than the picking error. Therefore, we are confident that trends in circle shoot data are not due to topography, and accurately reflect the material properties of the shallow subsurface.

4.2. Tomography

The average tomograms at the BR2 and BR3 sites suggest that the underlying CZ architecture is largely laterally homogenous over the scales of these surveys. This is inferred from the fact that all four models exhibit velocity gradients that are relatively strong normal to topography, but weak in the surface parallel direction (Figure 4). Furthermore, the lateral homogeneity of these models lends confidence that the sinusoidal travel time patterns presented in Figure 3 result from anisotropy rather than lateral heterogeneity.

These models present p-wave velocities that range from 400 to 3,000 m/s. Additionally, model variability resulting from the construction of average tomograms is relatively low (the standard deviation tends to be less than 100 m/s) across all tomograms, and is consistently higher toward the bottom of the models (Figure S4). This may be due to denser ray coverage in the upper portion of models, implying that increased ray coverage helps limit bias resulting from arbitrarily choosing an initial velocity model for inversion. Conversely, areas with low ray coverage may be more biased toward the initial model.

A_v values for both the BR2 and BR3 sites are low at shallow depths but increase until peak values of 33% and 31% respectively are reached at intermediate depths between 8 and 9 m bgs (Figure 5b). The A_v versus depth function associated with the BR2 and BR3 sites initially increase at similar rates, and at both sites, peak values are reached around 8 m depth. At both sites, after the peak is reached, anisotropy decreases with depth, declining to about 12% at 20 m depth at BR3, and vanishing entirely below 13 m at BR2 (Figure 5b).

4.3. Borehole Logs

Data from the borehole drilled and logged at the PB1 site allow us to catalog the rock fabric thought to cause seismic anisotropy. For instance, the attitude of foliation planes distinguished in the borehole logs generally match those collected by Crowley et al. (1975), in that planes strike roughly east-west and dip moderately (i.e., 20º) (Figure 6a). Additionally, numerous fractures possessing a similar orientation to that of the foliation planes (class I) are observed (Figure 6b). These fractures occur frequently throughout the borehole and have relatively small apertures, making them easier to identify with the acoustic log. Another class of fractures have larger apertures and appear to be filled with clay and oxidized minerals (class II), making them easy to identify with the optical log. The second class of fractures are not as uniformly oriented as the first, but contain many fractures which dip significantly steeper. Additionally, the strikes of these fractures tend to align well with the fast direction of anisotropy (Figure 6c).

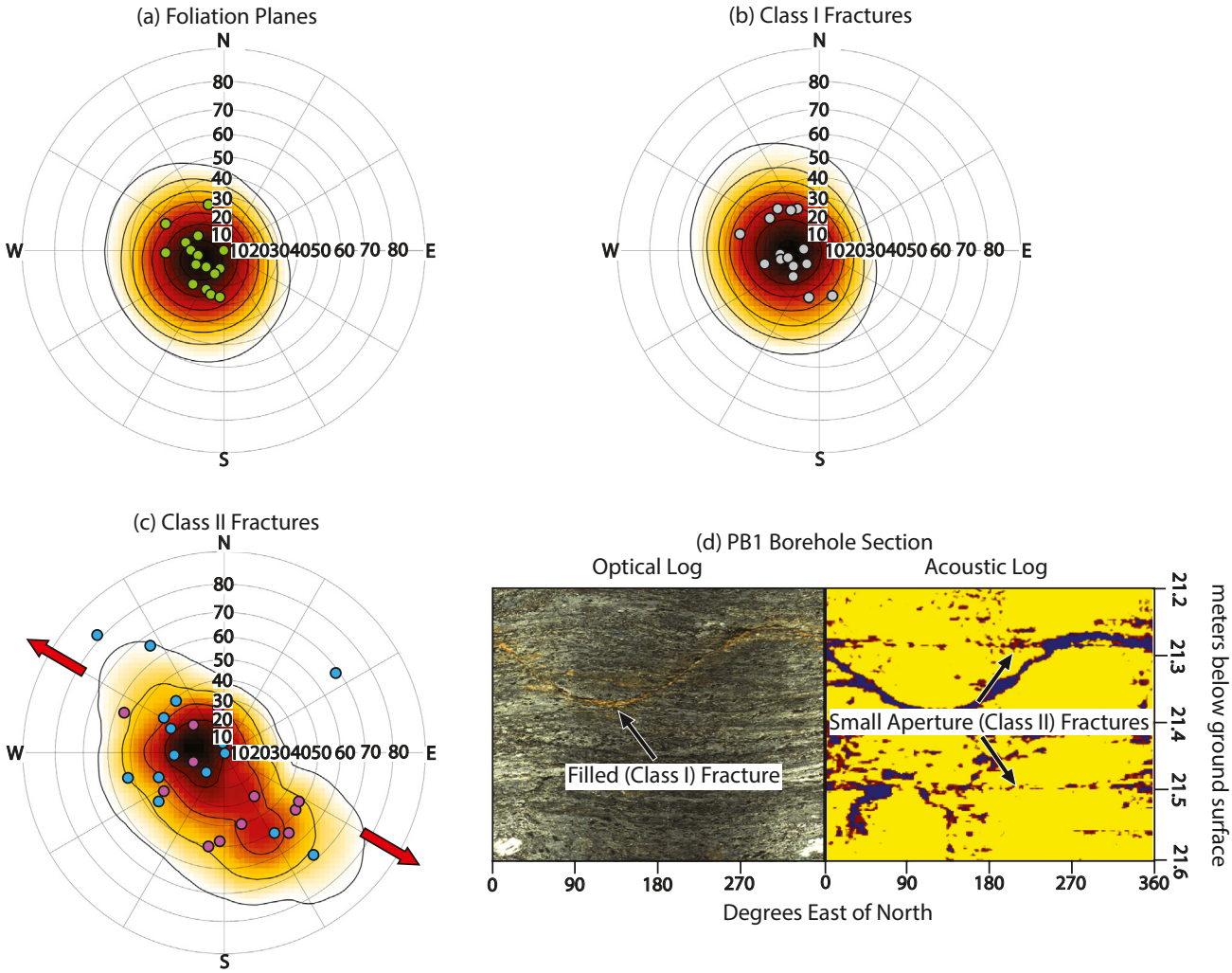

Figure 6. (a–c) Orientations of various structural features throughout the borehole. Note that these plots are not stereonets, but rather polar scatter plots where the radial variable corresponds to the dip magnitude and the azimuthal variable to strike direction. The Colored dots indicate the strike and dip magnitudes of planar features. Contour lines correspond to the number of standard deviations away from the expected value of the data being plotted, assuming a normal probability distribution. Likewise, shading relates to a probability density function derived from the data, with darker colors relating to higher probabilities. (a) Orientation of foliation planes picked with the borehole logs. (b) Orientations of small-aperture class I fractures. (c) Purple and blue poles correspond to the orientations of large-aperture class II fractures classified as open and partially open respectively. The red arrows point in the fast direction of anisotropy measured with the 25 m offset array at the PB1 site. (d) An example section from the PB1 borehole televiewer logs used to distinguish class I (small aperture) and II (filled) fractures (21.2–21.6 m bgs).

5. Discussion

In this study, we observed how rock fabric changes as a result of weathering by gauging seismic anisotropy variations with depth. We used methods based on radial surveys, originally employed by Novitsky et al. (2018), as well as a tomography-based method. In the first section of the discussion, we summarize our results from these methods and build on past studies to argue that in situ weathering may enhance seismic anisotropy. One such in-situ weathering process may be fracturing, and we go on to discuss how fractures observed in the borehole relate to the seismic anisotropy measured at the surface. Next, we assess the role that topographic stresses may play in inducing fracturing. We do this by using the topographic stress field at the location of the borehole to calculate at which orientations is fracturing most likely to occur and comparing these results with our findings from the borehole. In doing so, we attempt to ascribe a mechanism responsible for the high magnitudes of anisotropy observed in this study. We also discuss how chemical

weathering may be related to anisotropy enhancement and relay what the hydrologic and geomorphological implications of our work may be.

5.1. Depth-Dependent Anisotropy in Weathered Materials

The magnitudes of anisotropy observed at various depths in this study suggest that in situ weathering processes enhance anisotropy in bedrock material during exhumation toward the surface. This assertion is supported by data implying that magnitudes of anisotropy measured in saprolite and highly weathered bedrock tend to be larger than those measured in the less weathered bedrock below. For example, velocity tomograms (Figure 4) show that the seismic velocities at depths where anisotropy is highest (8–9 m bgs) are commensurate with those of saprolite and highly weathered bedrock (700–1,200 m/s) (e.g., Flinchum et al., 2019; Klos et al., 2018). Below this material, increasing seismic velocity implying progressively less weathered bedrock (e.g., Befus et al., 2011; Flinchum et al., 2019; Holbrook et al., 2014; St. Clair et al., 2015) is usually coincident with lower anisotropy values (Figures 4 & 5). At shallower depths where seismic velocities match that of soil (<500 m/s), anisotropy is absent, signifying a loss of rock structure, likely due to processes such as pore space collapse (e.g., Mathé et al., 1999), bioturbation, and freeze and thaw (Anderson et al., 2013).

Estimating the magnitude of seismic anisotropy caused by foliation is necessary to further evaluate the hypothesis that weathering enhances anisotropy. Unfortunately, the surveys in this study have relatively short offsets that do not sample intact bedrock at depth. This assertion can be made with confidence because the maximum observed seismic velocities in tomograms are 3,000 m/s (Figure 4), while St. Clair et al. (2015) observed velocities as high as to 5,000 m/s in their tomography surveys at Pond Branch. Nevertheless, lab measurements conducted on un-weathered samples of schist bedrock by Godfrey et al. (2000) may provide the necessary information to estimate the anisotropy of unweathered Loch Raven schist. Seismic anisotropy of the Haast, Pelona, and Coldfoot schists were measured under 100 MPa of pressure and exhibit maximum magnitudes of anisotropy of 16.5%, 16.8%, and 16.0% respectively (Godfrey et al., 2000). Of the three schists studied in Godfrey et al. (2000), the Pelona schist is most mineralogically similar to the Loch Raven, and thus, the ranges of anisotropy for this sample act as the best available estimate for the anisotropy of unweathered Loch Raven schist.

The dip angles of foliation planes relative to topography also influence the magnitude of seismic anisotropy measurable at the surface. Specifically, the maximum possible anisotropy values will be observed when the rock fabric and surface topography are perpendicular. As the angle of intersection between rock fabric and topography decreases, so does the measured magnitude of anisotropy (Novitsky et al., 2018; Okaya & McEvilly, 2003). In fact, numerical experiments have shown that when the angle of intersection is less than 45º, the observed magnitude of anisotropy can be reduced by more than a third (Novitsky et al., 2018). Throughout the Pond Branch and Baismen Run catchments, the angle of intersection between foliation and the topography is typically 20–30°. Hence, due to the moderate dips of foliation planes, the maximum amount of seismic anisotropy attributable to unweathered rock fabric is likely less than the largest values recorded by Godfrey et al. (2000). Therefore, it is likely that the original rock fabric has been altered significantly or, that some other type of fabric exists throughout in-place regolith which enhances anisotropy, helping account for magnitudes as high as 31% and 36% for A_v and A_t respectively. Moreover, if a second planar fabric is extant throughout the regolith, it must have a similar strike to those of the foliation planes. This is because the orientation of the fast direction remains roughly aligned with the strike of foliation planes, even when magnitudes of anisotropy are larger than what could reasonably be attributed to exclusively foliation (Table 1).

Examples of such fabric are found in the logs of the PB1 borehole. From these data, we can infer that the fractures along and subparallel to foliation planes (class I) likely enhance the anisotropic signal caused by foliation and inherited foliation-like structure in weathered bedrock and saprolite. This is attributed to their frequent occurrence as well as being aligned with foliation and relatively well with the fast direction of anisotropy. Moreover, the larger aperture clay-filled fractures (class II) may have an even greater effect on the anisotropic signal observed at this site. This is because these fractures are aligned even better with the fast direction of anisotropy while probably being significantly more seismically visible given their steep dips and wider openings.

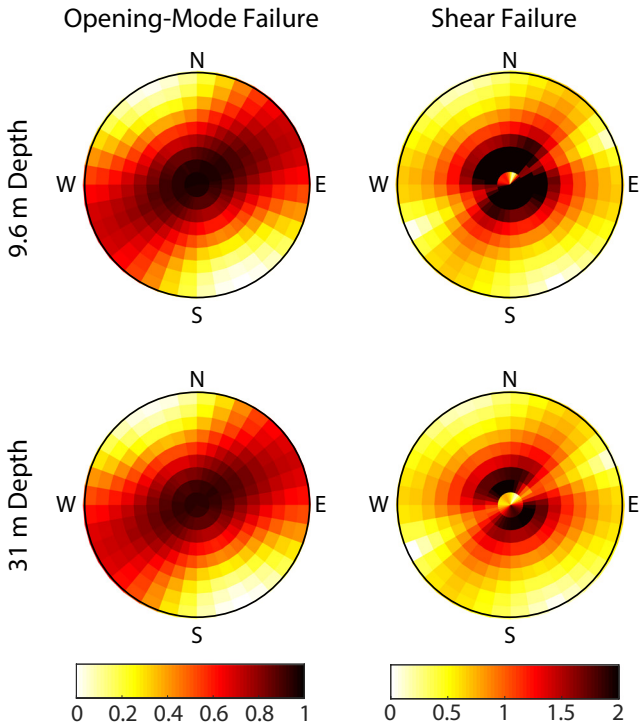

Figure 7. Polar plots colored to represent the magnitude of failure potential on planes of various strike and dip angles. Alike to Figure 6, the radial variable corresponds to the dip magnitude (0º dip being at the center and 90º being at the edge of the circle) and the azimuthal variable to strike direction. Both opening-mode and shear failure potentials are presented, each at two distinct depths that span the area over which borehole fractures were analyzed. Note that shear failure potential tends to be higher close to the surface, indicating a greater likelihood of fracture activation. Also, that the relative magnitudes of failure potential for any range of strike and dip angles is similar over this depth range.

5.2. Assessing the Influence of Topographic Stresses on Fracture Populations

The previous section provides evidence that fractures enhance anisotropy in weathered bedrock. Furthermore, related features likely also exist in the overlying saprolite as inherited fracture fabric and have a similar anisotropy enhancing effect (Novitsky et al., 2018). Therefore, understanding the mechanisms that could potentially induce fractures, such as those observed in Figure 6, would further elucidate how rock fabric weathers in the CZ. One potential mechanism for producing fractures are topographic stresses resulting from interactions between topography and regional tectonic stresses (Moon et al., 2017; St.Clair et al., 2015). To account for topographic stresses, it is necessary to calculate subsurface stress fields as the sum of ambient stresses due to tectonics and gravitational stress perturbations due to topography (Moon et al., 2017; Slim et al., 2015; St. Clair et al., 2015). This methodology has been applied to calculate the stress fields in Pond Branch (St. Clair et al., 2015), where the magnitudes of the most and least compressive horizontal stresses (σ_H and $\sigma_{h,}$ respectively) are estimated to be 10 and 3 MPa, with σ_H oriented N65ºE (Haimson & Doe, 1983; Palmer & Lo, 1978; Slim et al., 2015) (Figure 1). St. Clair et al. (2015) showed that topographic stress fields under strong compression may influence the occurrence of fractures and bulk weathering at the Pond Branch catchment. Their evidence for this included using the topographic stresses to calculate spatial variations in opening-mode and shear fracture potential, showing that the predicted surface-mirroring patterns of these failure proxies correlated well with observed seismic velocity profiles.

Here, we extracted subsurface stress fields at the PB1 borehole location from the 3D stress fields derived by St. Clair et al. (2015). Then, we calculated proxies of both shear and opening-mode failure potential on fracture planes of varying strikes and dips, following methods detailed by Moon et al. (2020). The proxy for shear failure potential is calculated as shear traction (τ) divided by normal traction (σ_n) on the fracture surface. The proxy for opening-mode failure potential is calculated as $(\sigma_{mcs} - \sigma_n)/\sigma_{mcs}$, the difference between the most compressive principal stress (σ_{mcs}) and the normal traction on the fracture surface, divided by σ_{mcs}. Higher failure proxies represent greater likelihoods of shear- or opening-mode failure on planes. Calculations of shear and opening–mode failure potentials from 10 and 31 m bgs at the PB1 borehole location are shown in Figure 7.

Several key findings are derived by comparing fracture potential, borehole observations, and the seismic anisotropy observed at the PB1 site. First, opening-mode failure potential is high on planes with gentle dips overall, as well as on steeply dipping planes that strike parallel to σ_H and perpendicular to σ_h. Therefore, foliation planes tend to experience high opening-mode failure potential near the surface. This suggests that failure along fractures oriented the same as foliation (e.g., Class I) may be promoted by topographic stresses (Figure 6b). Second, shear failure potential tends to be high on planes with gentle dips as well as on steeply dipping planes that strike in between σ_H and σ_h. Moreover, patterns in shear failure potential are better aligned with Class II fractures, particularly for fractures with steep dips striking oblique to σ_H. It is also notable that the direction in which shear failure potential is highest somewhat aligns with the fast direction of seismic anisotropy at BR1 (cf., 110º and 120º respectively).

The comparison between predicted and observed fracture patterns based on one borehole location shows a potential connection between topographic stresses and fracture populations. Interestingly, due to the highly compressive, strong anisotropic horizontal tectonic stresses in this area (σ_H = 10 MPa, σ_h = 3 MPa, H = N65ºE), topographic perturbation is not large enough to change the orientation of most compressive stress significantly. Thus, the relative distribution of modeled opening and shear failure potential on fracture

planes do not vary significantly on the ridge top locations where we perform circular surveys. Hence, the same relationship between failure potential and the fast direction of wave propagation observed at PB1 likely explains those observed at other survey sites as well.

While such results are promising, additional information is needed to better assess how topographic stresses are related to near-surface anisotropy. For example, fracture populations/characteristics from various positions across the landscape will help to assess the influence of topographic stresses on open fracture patterns more robustly. Also, previous studies have shown that failure tends to occur along foliation planes under most stress states (Basu et al., 2013; Kwasniewski & Mogi,, 2000). The current stress model and failure potential calculations assume isotropic rock material, which can be improved in the future by considering the anisotropic strength of the schist bedrock (e.g., Nasseri et al., 2002; Saeidi et al., 2014). Furthermore, it is possible that other weathering processes besides fracturing may influence the seismic anisotropy of weathered materials.

5.3. Linkages Between Weathering and Anisotropy

In this study, the highest magnitudes of anisotropy occur in saprolite and highly weathered bedrock (Figures 4 & 5). Saprolite at Oregon Ridge Park retains the original foliated rock fabric despite certain minerals (oligoclase and biotite) being replaced with clays, while others (quartz) remain in the regolith column (Cleaves et al., 1970; Goldich, 1938). Thus, in situ weathered material may now consist of alternating quartz and clay lamellae rather than quartz and biotite. Since clays have lower seismic velocities than the minerals they replace (Hall & Al-Haddad, 1979; Schumann et al., 2014), the addition of clays may contribute to the observed changes in seismic anisotropy at this site. However, the generation of porosity or void space would be expected to contribute even more to the overall anisotropy as air and water have lower seismic velocities than most weathered mineral products. Chemical weathering often generates volumetric expansion during mineral alteration which can also act to increase aperture between foliation planes resulting in increased anisotropy. Furthermore, biotite reacting with water to form clays may cause expansion perpendicular to cleavage planes, inducing microfracturing (e.g., Fordham, 1990; Gu et al., 2020; Marques et al., 2010; Rich, 1956; Shen et al., 2019) also resulting in enhanced anisotropy.

Nonetheless, it is important to emphasize that chemical weathering along the foliation cannot completely account for the seismic anisotropy variations we observed primarily because the foliation dips only moderately, meaning that surficial circular surveys do not optimally sample the foliation. To optimally sample the foliation, the rock fabric would have to be perpendicular to the ground surface. Novitsky at al. (2018) demonstrate this concept in their supporting information using numerical models to show that the magnitude of anisotropy measured using surficial arrays diminishes as the foliation planes and ground surface become more parallel. Additionally, steeper dipping class II fractures observed in the borehole tend to have large apertures and likely enhance seismic anisotropy. Thus, the anisotropy enhancement noted in this study must be at least partially attributed to changes in fracture density and/or opening apertures of steeply dipping fractures throughout the weathered profile.

5.4. Implications for Enhanced Anisotropy in the CZ

Our study may have broader implications if enhanced seismic anisotropy signifies enhancement of other kinds of anisotropy in weathered materials. Namely, permeability and rock strength may be of note. Schists are known to exhibit strength anisotropy, in that for many stress states, failure is more likely to occur along foliation planes (Basu et al., 2013; Kwasniewski & Mogi,, 2000). Thus, strength anisotropy plays a role in landscape evolution and hazard analysis because strength anisotropy may determine the depth and direction of slope failure (e.g., Glastonbury & Fell, 2010). Additionally, there are hydrologic implications as unweathered schists are known to exhibit preferential flow along foliation planes (Domenico & Schwartz, 1990). Therefore, weathering processes such as fracturing caused by topographic stresses and microcracking caused by biotite expansion likely enhance permeability anisotropy - similar to how those processes enhance seismic anisotropy. Further studies are needed to examine potential feedbacks between permeability anisotropy and chemical mass losses in foliated rocks and then link these observations to seismic anisotropy measurements.

6. Conclusions

In this study, seismic anisotropy is measured using both circular arrays of geophones and crossing seismic refraction profiles at four sites within Oregon Ridge Park. Our data show that anisotropy varies with depth, in that highly weathered bedrock and saprolite tend to be more anisotropic than the less weathered material below, while soil exhibits virtually no anisotropy. From this, it can be inferred that seismic anisotropy is enhanced by in situ weathering and eliminated by near surface mixing processes. An in situ weathering process that could serve to amplify anisotropy is fracturing along and subparallel to foliation planes caused by topographic/tectonic stresses. Other processes may include the preferential weathering of biotite and oligoclase out of the schist matrix and microcracking caused by biotite expansion. Nevertheless, the implication that weathering enhances seismic anisotropy lays the groundwork for a promising new vein of research with hydrological and geomorphic implications. This is because if weathering enhances seismic anisotropy, it seems reasonable to predict that other types of anisotropy may also be enhanced, namely permeability and rock strength.

Data Availability Statement

All ground motion data collected at sites PB1, BR1, BR2, and BR3 are available on the CUAHSI managed online database HydroShare at (https://www.hydroshare.org/resource/541124a1dbca409fb6a29b8f35fb3c01/).

Acknowledgments
The authors are very thankful for the services of William Irving, Shane Putnam, and Rob Dean, who helped with data collection, as well as to administrators at the Oregon Ridge Nature Center for their permission and support in conducting field work. Thanks are also extended to the Dickinson College Research and Development Committee as well as the William Vernon and Robert Jansen Research Funds for helping support this research. This project was also funded by NSF-EAR 20–12316 to J. L. Hayes, 19–45431 and 20–12073 to S. Moon, 1654194 to C. J. Harman, and 2012353 to W. S. Holbrook.

References

Anderson, R. S., Anderson, S. P., & Tucker, G. E. (2013). Rock damage and regolith transport by frost: An example of climate modulation of the geomorphology of the critical zone. *Earth Surface Process. Landforms*, *38*, 299–316. https://doi.org/10.1002/esp.3330

Anderson, S. P., Von Blanckenburg, F., & White, A. F. (2007). Physical and chemical controls on the critical zone. *Elements*, *3*(5), 315–319. https://doi.org/10.2113/gselements.3.5.315

Barton, N. (2006). *Rock Quality, seismic velocity, attenuation and anisotropy*. London: Taylor and Francis Group.

Basu, A., Mishra, D. A., & Roychowdhury, K. (2013). Rock failure modes under uniaxial compression, Brazilian, and point load tests. *Bulletin of Engineering Geology and the Environment*, *72*, 457–475. https://doi.org/10.1007/s10064-013-0505-4

Befus, K., Sheehan, A., Leopold, M., Anderson, S., & Anderson, R. (2011). Seismic constraints on critical zone architecture, Boulder Creek watershed, Front Range, Colorado. *Vadose Zone Journal*, *10*, 915–1342. https://doi.org/10.2136/vzj2010.0108er

Birch, F. (1960). The velocity of compressional waves in rocks to 10 kilobars. *Journal of Geophysical Research*, *65*, 1083–1102. https://doi.org/10.1029/jz065i004p01083

Brantley, S. L., Goldhaber, M. B., & Ragnarsdottir, K. V. (2007). Crossing disciplines and scales to understand the critical zone. *Elements*, *3*, 307–314. https://doi.org/10.2113/gselements.3.5.307

Brantley, S. L., Lebedeva, M. I., Balashov, V. N., Singha, K., Sullivan, P. L., & Stinchcomb, G. (2016). Toward a conceptual model relating chemical reaction fronts to water flow paths in hills. *Geomorphology*. https://doi.org/10.1016/j.geomorph.2016.09.027

Buss, H. L., Sak, P. B., Webb, S. M., & Brantley, S. L. (2008). Weathering of the Rio Blanco quartz diorite, Luquillo Mountains, Puerto Rico: Coupling oxidation, dissolution, and fracturing. *Geochimica et Cosmochimica Acta*, *72*(18), 4488–4507. https://doi.org/10.1016/j.gca.2008.06.020

Cleaves, E. T., Godfrey, A. E., & Bricker, O. P. (1970). Geochemical balance of a small watershed and its geomorphic implications. *Geological Society of America*, *81*(10), 3015–3032. https://doi.org/10.1130/0016-7606(1970)81[3015:GBOASW]2.0.CO;2

Crampin, S. (1984). Effective anisotropic elastic constants for wave propagation through cracked solids. *Geophysical Journal of the Royal Astronomical Society*, *76*(1), 135–145. https://doi.org/10.1111/j.1365-246X.1984.tb05029.x

Crampin, S., McGonigle, R., & Bamford, D. (1980). Estimating crack parameters from observations of *P*-wave velocity anisotropy. *Geophysics*, *45*, 345–360. https://doi.org/10.1190/1.1441086

Crowley, W. P., Reinhardt, J., & Cleaves, T. E. (1975). *Geologic map of the Cockeysville quadrangle, Maryland, U.S, (Quadrangle Atlas QA-3, scale 1:24,000)*. Geological Survey. https://doi.org/10.1180/claymin.2007.042.4.01

Domenico, P. A., & Schwartz, F. W. (1990). *Physical and chemical hydrogeology*. New York: Wiley.

Duncan, J. M., Groffman, P. M., & Band, L. E. (2013). Towards closing the watershed nitrogen budget : Spatial and temporal scaling of denitrification. *Journal of Geophysical Research: Biogeosciences*, *118*, 1105–1119. https://doi.org/10.1002/jgrg.20090

Fahey, B. D. (1983). Frost action and hydration as rock weathering mechanisms on schist: A laboratory study. *Earth Surface and Process Landforms*, *8*, 535–545. https://doi.org/10.1002/esp.3290080605

Fletcher, R. C., Buss, H. L., & Brantley, S. L. (2006). A spheroidal weathering model coupling pore water chemistry to soil thicknesses during steady state erosion. *Earth and Planetary Science Letters*, *244*(1–2), 444–457. https://doi.org/10.1016/j.epsl.2006.01.055

Flinchum, B. A., Holbrook, W. S., Parsekian, A. D., & Carr, B. J. (2019). Characterizing the critical zone using borehole and surface nuclear magnetic resonance. *Vadose Zone Journal*, *18*, 1–18. https://doi.org/10.2136/vzj2018.12.0209

Flinchum, B. A., Holbrook, W. S., Rempe, D., Moon, S., Riebe, C. S., Carr, B. J., et al. (2018). Critical zone structure under a granite ridge inferred from drilling and three-dimensional seismic refraction data. *Journal of Geophysical Research: Earth Surface*, *123*, 1317–1343. https://doi.org/10.1029/2017jf004280

Fordham, A. W. (1990). Weathering of biotite into dioctahedral clay-minerals. *Clay Minerals*, *25*, 51–63. https://doi.org/10.1180/claymin.1990.025.1.06

Gerke, H. H., & Vangenuchten, M. T. (1993). A dual-porosity model for simulating the preferential movement of water and solutes in structured porous-media. *Water Resources Research*, *29*(2), 305–319. https://doi.org/10.1029/92WR02339

Glastonbury, J., & Fell, R. (2010). Geotechnical characteristics of large rapid rock slides. *Canadian Geotechnical Journal*, *47*, 116–132. https://doi.org/10.1139/T09-080

Godfrey, N. J., Christensen, N. I., & Okaya, D. A. (2000). Anisotropy of schists: Contribution of crustal anisotropy to active source seismic experiments and shear wave splitting observations. *Journal of Geophysics Research*, *105*(B12), 27991–28007. https://doi.org/10.1029/2000JB900286

Goldich, S. S. (1938). A study in rock-weathering. *The Journal of Geology*, *46*(1), 17–58. https://doi.org/10.1086/624619

Gu, X., Rempe, D. M., Dietrich, W. E., West, A. J., Lin, T. C., Jin, L., & Brantley, S. L. (2020). Chemical reactions, porosity, and microfracturing in shale during weathering: The effect of erosion rate. *Geochimica et Cosmochimica Acta*, *269*, 63–100. https://doi.org/10.1016/J.GCA.2019.09.044

Haimson, B. C., & Doe, T. W. (1983). State of stress, permeability, and fractures in the Precambrian granite of northern Illinois. *Journal of Geophysical Research*, *88*(B9), 7355–7371. https://doi.org/10.1029/JB088iB09p07355

Hall, J., & Al-Haddad, F. M. (1979). Variation of effective seismic velocities of minerals with pressure and its use in velocity prediction. *Geophysical Journal International*, *57*(1), 107–118. https://doi.org/10.1111/j.1365-246X.1979.tb03775.x

Harman, C. J., & Cosans, C. L. (2019). A low-dimensional model of bedrock weathering and lateral flow co-evolution in hillslopes: 2. Controls on weathering and permeability profiles, drainage hydraulics, and solute export pathways. *Hydrological Processes*, *33*, 1168–1190. https://doi.org/10.1002/hyp.13385

Hayes, J. L., Riebe, C. S., Holbrook, W. S., Flinchum, B. A., & Hartsough, P. C. (2019). Porosity production in weathered rock: Where volumetric strain dominates over chemical mass loss. *Science Advances*, *5*(9), eaao0834. https://www.science.org/doi/10.1126/sciadv.aao0834

Holbrook, W. S., Marcon, V., Bacon, A. R., Brantley, S. L., Carr, B. J., Flinchum, B. A., et al. (2019). Links between physical and chemical weathering inferred from a 65-m-deep borehole through Earth 's critical zone. *Scientific Reports*, *9*(1). https://doi.org/10.1038/s41598-019-40819-9

Holbrook, W. S., Riebe, C. S., Elwaseif, M., Hayes, J. L., Harry, D. L., Basler-Reeder, K., et al. (2014). Geophysical constraints on deep weathering and water storage potential in the Southern Sierra Critical Zone Observatory. *Earth Surface Processes and Landforms*, *39*, 366–380. https://doi.org/10.1002/esp.3502

Klos, P. Z., Goulden, M. L., Riebe, C. S., Tague, C. L., O'Geen, A. T., Flinchum, B. A., et al. (2018). Subsurface plant-accessible water in mountain ecosystems with a Mediterranean climate. *Wiley Interdisciplinary Reviews: Water*. https://doi.org/10.1002/wat2.1277

Kwasniewski, M. A., & Mogi, K. (2000). *Faulting in an anisotropic, schistose rock under general triaxial compression*. American Rock Mechanics Association.

Leone, J. D., Holbrook, W. S., Riebe, C. S., Chorover, J., Ferré, T. P. A., Carr, B. J., & Callahan, R. P. (2020). Strong slope-aspect control of regolith thickness by bedrock foliation. *Earth Surface Processes and Landforms*, *45*, 2998–3010. https://doi.org/10.1002/esp.4947

Marques, E. A. G., Barroso, E. V., Filho, A. P. M., & Jr, E. A. V. (2010). Weathering zones on metamorphic rocks from Rio de Janeiro — Physical, mineralogical and geomechanical characterization. *Engineering Geology*, *111*(1–4), 1–18. https://doi.org/10.1016/j.enggeo.2009.11.001

Mathé, P.-E., Rochette, P., Vandamme, D., & Colin, F. (1999). Volumetric changes in weathered profiles: Iso-element mass balance method questioned by magnetic fabric. *Earth and Planetary Science Letters*, *167*, 255–267. https://doi.org/10.1016/s0012-821x(99)00024-2

Meunier, A., Sardini, P., Robinet, J. C., & Pret, D. (2007). The petrography of weathering processes: Facts and outlooks. *Clay Minerals*, *42*(4), 415–435. https://doi.org/10.1180/claymin.2007.042.4.01

Moon, S., Perron, J. T., Martel, S. J., Goodfellow, B. W., Mas Ivars, D., Hall, A., et al. (2020). Present-day stress field influences bedrock fracture openness deep into the subsurface. *Geophysical Research Letters*, *47*, e2020GL090581. https://doi.org/10.1029/2020GL090581

Moon, S., Perron, J. T., Martel, S. J., Holbrook, W. S., & St. Clair, J. (2017). A model of three-dimensional topographic stresses with implications for bedrock fractures, surface processes, and landscape evolution. *Journal of Geophysical Research: Earth Surface*, *122*, 823–846. https://doi.org/10.1002/2016JF004155

Nasseri, M. H. B., Rao, K. S., & Ramamurthy, T. (2002). Anisotropic strength and deformational behavior of Himalayan schists. *International Journal of Rock Mechanics and Mining Sciences*, *40*(1), 3–23. https://doi.org/10.1016/S1365-1609(02)00103-X

Navarre-Sitchler, A., Brantley, S. L., & Rother, G. (2015). How porosity increases during incipient weathering of crystalline silicate rocks. *Reviews in Mineralogy and Geochemistry*, *80*(1), 331–354. https://doi.org/10.2138/rmg.2015.80.10

Neuman, S. P. (2005). Trends, prospects and challenges in quantifying flow and transport through fractured rocks. *Hydrogeology Journal*, *13*(1), 124–147. https://doi.org/10.1007/s10040-004-0397-2

Novitsky, C. G., Holbrook, W. S., Carr, B. J., Pasquet, S., Okaya, D., & Flinchum, B. A. (2018). Mapping Inherited Fractures in the Critical Zone Using Seismic Anisotropy From Circular Surveys. *Geophysical Research Letters*, *45*, 3126–3135. https://doi.org/10.1002/2017gl075976

Nutter, L. J., & Otton, E. G. (1969). Ground-water Occurrence in the Maryland Piedmont. *Maryland Geological Survey Report of Investigations*.

Okaya, D. A., & Christensen, N. I. (2002). Anisotropic effects of non-axial seismic wave propagation in foliated crustal rocks. *Geophysical Research Letters*, *29*(11). https://doi.org/10.1029/2001GL014285

Okaya, D. A., & McEvilly, T. V. (2003). Elastic wave propagation in anisotropic crustal material possessing arbitrary internal tilt. *Geophysical Journal International*, *153*, 344–358. https://doi.org/10.1046/j.1365-246x.2003.01896.x

Palmer, J. H. L., & Lo, K. Y. (1978). In-situ stress measurements in some near surface rock formations, Thorold, Ontario. *Canadian Geotechnical Journal*, *13*, 179–182

Rempe, D. M., & Dietrich, W. E. (2014). A bottom-up control on fresh-bedrock topography under landscapes. *Proceedings of the National Academy of Sciences*, *111*(18), 6576–6581. https://doi.org/10.1073/pnas.1404763111

Rich, C. I. (1956). Muscovite weathering in a soil developed in the Virginia Piedmont. *Clays and Clay Minerals*, *5*, 203–212. https://doi.org/10.1346/CCMN.1956.0050117

Riebe, C. S., Hahm, W. J., & Brantley, S. L. (2017). Controls on deep critical zone architecture: A historical review and four testable hypotheses. *Earth Surface Processes and Landforms*, *42*, 128–156. https://doi.org/10.1002/esp.4052

Sacchi, M. D. (1998). A bootstrap procedure for high-resolution velocity analysis. *Geophysics*, *63*(5), 1716–1725. https://doi.org/10.1190/1.1444467

Saeidi, O., Rasouli, V., Vaneghi, R. G., Gholami, R., & Torabi, S. R. (2014). A modified failure criterion for transversely isotropic rocks. *Geoscience Frontiers*, *5*(2), 215–225. https://doi.org/10.1016/j.gsf.2013.05.005

Schumann, K., Stipp, M., Behrmann, J. H., Klaeschen, D., & Schulte-Kortnack, D. (2014). *P* and *S* wave velocity measurements of water-rich sediments from the Nankai Trough, Japan. *Journal of Geophysical Research: Solid Earth*, *119*, 787–805. https://doi.org/10.1002/2013JB010290

Shen, X., Arson, C., Ferrier, K. L., West, N., & Dai, S. (2019). Mineral weathering and bedrock weakening: Modeling microscale bedrock damage under biotite weathering. *Journal of Geophysical Research: Earth Surface*, *124*, 2623–2646. https://doi.org/10.1029/2019jf005068

Slim, M., Perron, J. T., Martel, S. J., & Singha, K. (2015). Topographic stress and rock fracture: A two-dimensional numerical model for arbitrary topography and preliminary comparison with borehole observations. *Earth Surface Processes and Landforms*, *40*(4), 512–529. https://doi.org/10.1002/esp.3646

Sowards, K. F., Nelson, S. T., McBride, J. H., Bickmore, B. R., Heizler, M. T., Tingey, D. D., et al. (2018). A conceptual model for the rapid weathering of tropical ocean islands: A synthesis of geochemistry and geophysics, Kohala Peninsula, Hawaii, USA. *Geosphere*, *14*(3), 1324–1342. https://doi.org/10.1130/GES01642.1

St. Clair, J., Moon, S., Holbrook, W. S., Perron, J. T., Riebe, C. S., Martel, S. J., et al. (2015). Geophysical imaging reveals topographic stress control of bedrock weathering. *Science*, *350*(6260), 534–538. https://doi.org/10.1126/science.aab2210

Zimmerman, R. W., & Bodvarsson, G. S. (1996). Hydraulic conductivity of rock fractures. *Transport in Porous Media*, *23*(1), 1–30. https://doi.org/10.1007/bf00145263